

Superconductivity protected by spin-valley locking in ion-gated MoS₂

Yu Saito*, Yasuharu Nakamura, Mohammad Saeed Bahramy, Yoshimitsu Kohama,

Jianting Ye, Yuichi Kasahara, Yuji Nakagawa, Masaru Onga, Masashi Tokunaga,

Tsutomu Nojima, Youichi Yanase and Yoshihiro Iwasa*

*Corresponding author. E-mail: saito@mp.t.u-tokyo.ac.jp (Y.S.); iwasa@ap.t.u-tokyo.ac.jp (Y.I.)

Contents

I. Possibility of electrochemical reaction

II. High magnetic field measurements

III. Possible origins for the enhancement of H_{c2}

IV. Tight-binding model

V. Numerical calculation of the Pauli limit

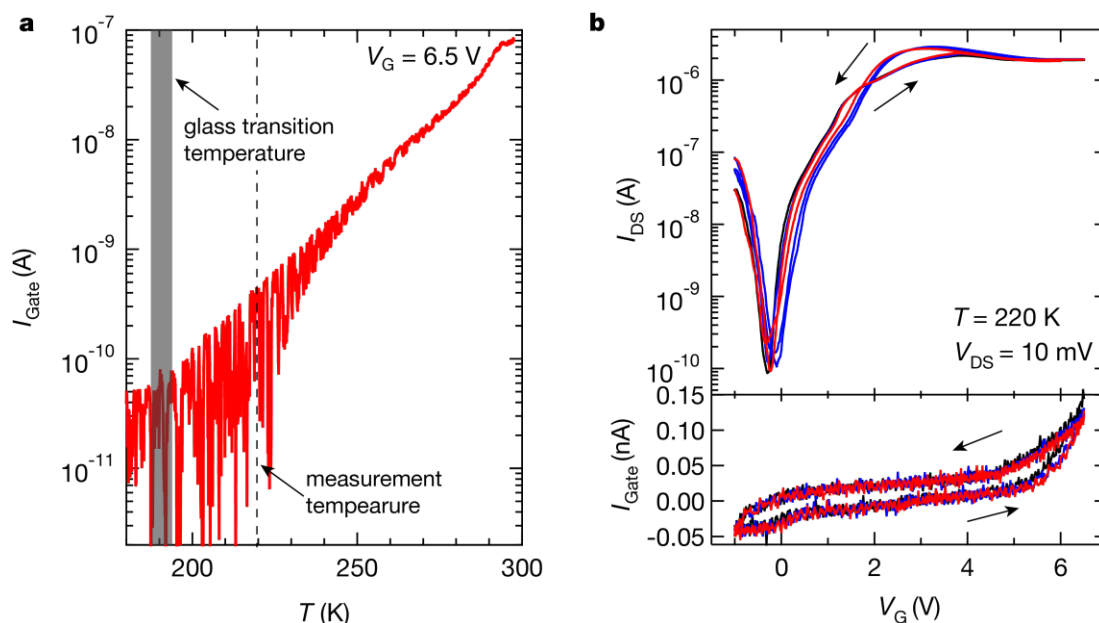
VI. Discrepancy between the theoretical results and experimental results

I. Possibility of electrochemical reaction

In the entire measurement, the electrochemical reaction can be excluded for the following reasons.

First of all, at low temperatures, especially just above the glass transition temperature of ionic liquid, which is approximately 190 K, the activation energy of electrochemical process is significantly suppressed. Supplementary Figure 1a displays the temperature dependent gate current, I_{Gate} , in a MoS₂-EDLT. I_{Gate} shows an activation-type reduction with temperature, with an activation energy of ~ 0.4 eV. This dramatic reduction of I_{Gate} upon lowering temperature suggests that the electrochemical window is effectively widened¹. Also, it has been reported that the maximum gate voltage applicable increases from 3 to 5.5 V, simply by decreasing temperature from 300 to 220 K².

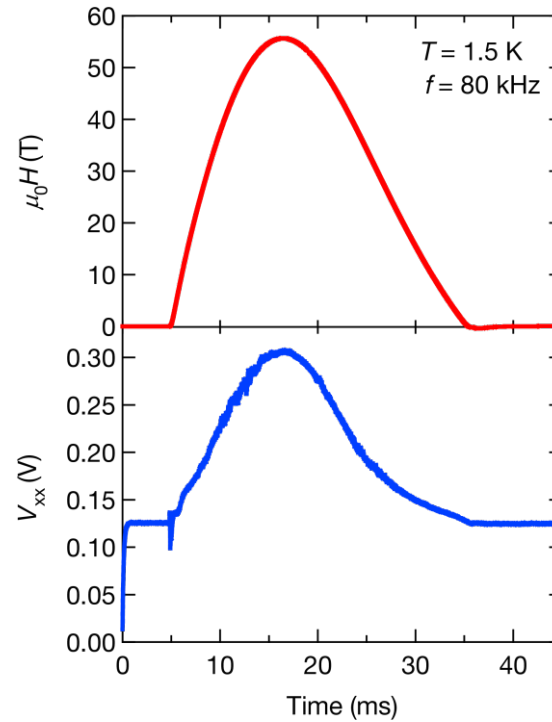
Furthermore, to confirm the electrostatic process of ionic-liquid gating, we measured transfer curves of a MoS₂-EDLT at 220 K. Supplementary Figure 1b shows the source-drain current, I_{DS} , and I_{Gate} as a function of gate voltage between -1 and 6.5 V. Both I_{DS} and I_{Gate} of the device completely returned back to the original values without large hysteresis. This is a strong indication that the ionic-liquid gating is a reversible process, and thus the electrochemical reaction is highly unlikely.



Supplementary Figure 1 | Temperature dependence of (a) the gate current I_{Gate} and (b) the transfer curve at 220 K of a MoS₂-EDLT.

II. High magnetic field measurements

We performed all the magnetoresistance measurements in a four-probe configuration using a 55 T pulsed magnet with the duration time of 36 ms and a rotator probe at the International MegaGauss Science Laboratory, Institute for Solid State Physics, the University of Tokyo. The voltage signals were recorded on National Instruments PXIe-6124 digitizers using a homemade numerical lock-in technique at a frequency of $f = 80$ kHz. The sensitivity of the angle measurement is within ~ 0.1 degree in our rotator probe. To align the field direction, we performed the H_{c2} measurement as a function of angle in pulsed magnetic fields. The misalignments for the in-plane magnetic fields and out-of-plane magnetic fields are estimated to be less than ~ 0.02 and ~ 1.0 degree, respectively. We observed clear voltage signals of the magnetoresistance from a MoS₂-EDLT, followed by pulsed magnetic fields. Supplementary Figure 2 shows a typical time dependent voltage signal under a pulsed magnetic field. The magnetoresistance data (shown in Fig. 3, a and b) was obtained during the down sweep of a field pulse with the field perpendicular to the c -axis. All these magnetoresistance measurements have been performed out under the condition that the source-drain current, I_{DS} , was less than $10 \mu\text{A}$, in which we confirmed that the behaviour of the temperature-dependent resistance and magnetoresistance below 8 K were almost unchanged. Some eddy current heating was observed in measurements between 4 and 8 K. Below 4 K, the MoS₂-EDLT was immersed in liquid helium, which prevents heating in the device.



Supplementary Figure 2 | Time-dependent magnetic field and voltage probe signal in a MoS₂-EDLT at $V_G = 5.5$ V. The upper and lower panels show a pulsed magnetic field and the voltage probe signal as a function of time, respectively. This measurement was made at $T = 1.5$ K with an AC measurement set up with a frequency of $f = 80$ kHz.

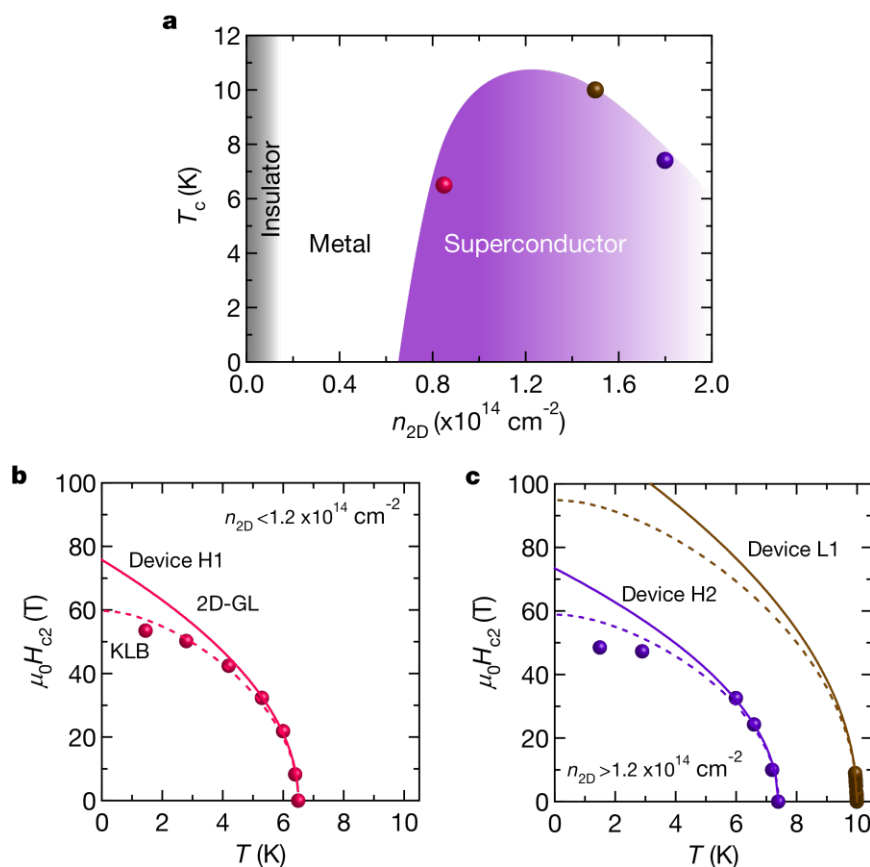
III. Possible origins of the enhancement of H_{c2}

1) Spin orbit scattering

To discuss spin orbit scattering effect on the enhancement of H_{c2} on MoS₂-EDLTs, we fitted $H_{c2}^{\parallel}(T)$ values of three devices (Device H1, H2, L1; those devices showed different T_c at different carrier densities (Supplementary Fig. 3a).) by using the microscopic KLB theory⁴. In this theory, $H_{c2}^{\parallel}(T)$ arising from a monolayer satisfies the following equations,

$$\ln\left(\frac{T}{T_c}\right) + \psi\left(\frac{1}{2} + \frac{3\tau_{SO}(\mu_B H_{c2}^{\parallel})^2}{4\pi T}\right) - \psi\left(\frac{1}{2}\right) = 0$$

where $\psi(x)$, μ_B and T_c are digamma function, the Bohr magnetism and T_c , respectively. Using this equation, we fitted the experimental data (Supplementary Fig. 3, b and c) and then estimated the values of τ_{SO} as a fitting parameter (Supplementary Table 1). Although all $H_{c2}^{\parallel}(T)$ values seem to be quite well fitted by the KLB theory, τ estimated by the transport is larger than τ_{SO} , being unphysical. Thus, spin orbit scattering is unlikely to be responsible for the enhancement of $H_{c2}^{\parallel}(T)$.



Supplementary Figure 3 | $H_{c2}^{\parallel}(T)$ values at different carrier densities and fitting results. a. Electronic phase diagram of ion-gated MoS₂. Here, T_c is determined at the temperature where the

resistance drop reaches 75% of its normal state sheet resistance R_N at 15 K. **b, c**, Temperature dependence of $H_{c2}^{\parallel}(T)$ at different carrier densities (**b**: $n_{2D} < 1.2 \times 10^{14} \text{ cm}^{-2}$, **c**: $n_{2D} > 1.2 \times 10^{14} \text{ cm}^{-2}$). Solid and dashed curves show the 2D-GL and the KLB fittings, respectively.

	T_c (K)	n_{2D} (cm^{-2})	μ_H (cm^2/Vs)	τ (fs)	τ_{SO} (fs)
Device L1	10.0	1.5×10^{14}	208	59.3	11.1
Device H1	6.5	0.85×10^{14}	86	25.5	17.9
Device H2	7.4	1.8×10^{14}	165	47.1	21.3

Supplementary Table 1 | Device properties of MoS₂-EDLTs. n_{2D} , Hall mobility, μ_H , and τ are values measured at 15 K.

2) Rashba SOI

Rashba spin-orbit coupling (SOC) will lock the spin to the in-plane direction, which can enhance the out-of-plane H_{c2} beyond the Pauli limit⁵. However, for in-plane magnetic fields, most of the electron spins can contribute to Pauli paramagnetism. Therefore, the enhancement of H_{c2} can be only $\sqrt{2}H_p^{\text{BCS}}$ ⁶. In the present case, H_{c2} is enhanced by a factor of 4, which is much larger than the enhancement due to the Rashba SOI. Furthermore, according to our calculations, the Rashba SOI is negligibly small in the present system, and thus the pure Rashba SOI effect does not contribute to the enhancement of H_{c2} .

3) Quantum critical point

No ordered state (ex. antiferromagnetic state) has been observed in ion-gated MoS₂ system in the vicinity of the superconducting phase. In that narrow sense, ion-gated MoS₂ system has no quantum critical point (QCP), which is known to dramatically enhance the upper critical field⁷. Thus, the enhancement of H_{c2} by the QCP can be ruled out.

4) Modified electron g-factor

The enhancement of upper critical fields owing to modified electron g-factor may become effective in the case that the LS coupling of multiple d -orbitals competing with crystal field splitting^{5, 8} stabilizes the spin-orbital coupled ground state. In the present system, the conduction band at the Fermi level is composed of only single d orbital (d_{z^2})⁹, and therefore, the effect of modified electron g-factor is supposed to be negligible.

IV. Tight-binding model

To calculate the subband structure of MoS₂ under a strong electric field, we first carried out density functional theory calculations for bulk MoS₂ using the full potential augmented plane-wave method and Perdew–Burke–Ernzerhof exchange–correlation functional modified by Becke–Johnson potential, as implemented in WIEN2K program¹⁰. For each atom, the muffin-tin radius, R_{MT} , was chosen such that its product with the maximum modulus of reciprocal vectors, K_{max} , becomes $R_{\text{MT}} K_{\text{max}} = 7.0$. The relativistic effects, including spin-orbit interaction were fully included and the Brillouin zone was sampled by a $12 \times 12 \times 6$ k -mesh. We then downfolded the bulk Hamiltonian using maximally localized Wannier functions^{11–13} and generated a large tight-binding supercell Hamiltonian with an additional potential term to account for the band bending. Finally, we solved this self-consistently using the Poisson equation.

The calculation of H_{c2}^{\parallel} was carried out based on the tight-binding model which reproduces the conduction band of the effectively single layer MoS₂. The single particle component of the Hamiltonian is given by $H = H_{\text{kin}} + H_Z + H_R$, where the first term is the kinetic energy term, $H_{\text{kin}} = \sum_{\mathbf{k}\mathbf{s}} \varepsilon(\mathbf{k}) c_{\mathbf{k}\mathbf{s}}^{\dagger} c_{\mathbf{k}\mathbf{s}}$. The dispersion relation obtained by the first-principles-based band structure calculation (shown in Fig. 4, a and b) is reproduced well by taking into account the nearest-, next-nearest-, and third-nearest-neighbour hopping,

$$\begin{aligned} \varepsilon(\mathbf{k}) = & 2t_1 \left(\cos k_y a + 2 \cos \frac{\sqrt{3}}{2} k_x a \cos \frac{1}{2} k_y a \right) \\ & + 2t_2 \left(\cos \sqrt{3} k_x a + 2 \cos \frac{\sqrt{3}}{2} k_x a \cos \frac{3}{2} k_y a \right) \\ & + 2t_3 \left(\cos 2k_y a + 2 \cos \sqrt{3} k_x a \cos k_y a \right) - \mu. \end{aligned}$$

where a is the lattice constant. We determined the hopping parameters t_1 , t_2 , and t_3 , and the chemical potential μ so as to reproduce the band structure calculation. The Zeeman-type SOI arising from the intrinsic inversion symmetry breaking in the crystal structure of MoS₂ is represented by H_Z , whereas the Rashba-type SOI induced by the extrinsic electric field is represented by H_R . They are characterized by the \mathbf{g} -vector as $H_Z = \alpha_Z \sum_{\mathbf{k}\mathbf{s}\mathbf{s}'} \mathbf{g}_Z(\mathbf{k}) \boldsymbol{\sigma}_{\mathbf{s}\mathbf{s}'} c_{\mathbf{k}\mathbf{s}}^{\dagger} c_{\mathbf{k}\mathbf{s}'}$ and $H_R = \alpha_R \sum_{\mathbf{k}\mathbf{s}\mathbf{s}'} \mathbf{g}_R(\mathbf{k}) \boldsymbol{\sigma}_{\mathbf{s}\mathbf{s}'} c_{\mathbf{k}\mathbf{s}}^{\dagger} c_{\mathbf{k}\mathbf{s}'}$, where

$$\mathbf{g}_Z(\mathbf{k}) = F(\mathbf{k}) \left(0, 0, \sin k_y a - 2 \cos \frac{\sqrt{3}}{2} k_x a \sin \frac{1}{2} k_y a \right), \text{ and}$$

$$\mathbf{g}_R(\mathbf{k}) = F(\mathbf{k}) \left(-\sin k_y a - \cos \frac{\sqrt{3}}{2} k_x a \sin \frac{1}{2} k_y a, \sqrt{3} \sin \frac{\sqrt{3}}{2} k_x a \cos \frac{1}{2} k_y a, 0 \right).$$

We introduced a trial function $F(\mathbf{k}) = \beta \tanh[f(\mathbf{K}) - f(\mathbf{k})] - 1$ in order to reproduce the sign change of the spin-splitting from the K point to the Γ point in the Brillouin zone. $\mathbf{K} = \left(0, \frac{4\pi}{3a} \right)$ is the wave vector at the K point. We chose the symmetric function

$$f(\mathbf{k}) = \left| \sin k_y a - 2 \cos \frac{\sqrt{3}}{2} k_x a \sin \frac{1}{2} k_y a \right| \text{ for simplicity. By diagonalizing the single particle}$$

Hamiltonian, we obtained the spin-split bands $E_+(\mathbf{k})$ and $E_-(\mathbf{k})$, and fitted parameters α_Z, α_R ,

and β to the results of band structure calculation, $E_+(\mathbf{k}_F) - E_-(\mathbf{k}_F) = 13 \text{ meV}$, $E_+(\mathbf{K}) - E_-(\mathbf{K}) = 3 \text{ meV}$ at $n_{2D} = 8.7 \times 10^{13} \text{ cm}^{-2}$, and the ratio of the Rashba- and Zeeman-type SOIs

$$\langle S_R \rangle / \langle S_Z \rangle = |\alpha_R \mathbf{g}_R(\mathbf{k}_F)| / |\alpha_Z \mathbf{g}_Z(\mathbf{k}_F)| = 0.02. \text{ The last equation relies on the results of } ab\text{-initio-based}$$

band calculations that the Rashba-type spin-splitting is at most 2% of the Zeeman-type

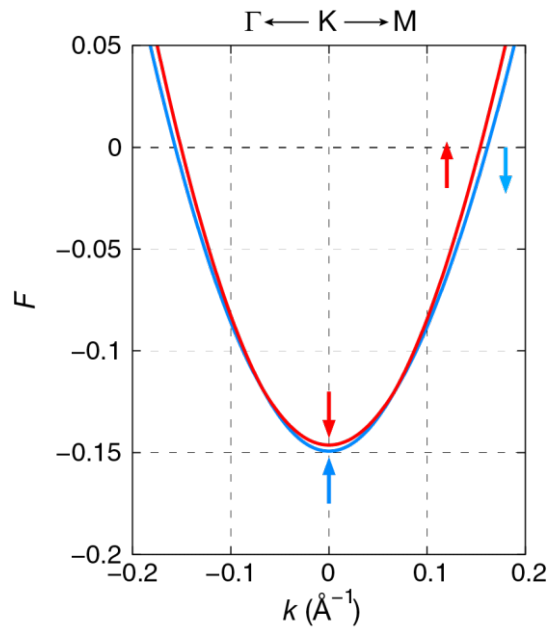
spin-splitting on the Fermi surface. We defined the Fermi momentum along the K-M line, \mathbf{k}_F ,

where $E_+(\mathbf{k}_F) + E_-(\mathbf{k}_F) = 0$. Adopting these parameters, we obtained the band structure in

Supplementary Fig. 4, which matches with Fig. 4b obtained by the band structure calculation for

the MoS₂-EDLT. In order to clarify the roles of Rashba-type SOI, we varied $\langle S_R \rangle / \langle S_Z \rangle$ from

0% to 10% in Fig. 4c.



Supplementary Figure 4 | Band structure near the K point reproduced by the tight-binding model. The horizontal axis shows the deviation from the K point, $\pm |\mathbf{k} - \mathbf{K}|$. The positive sign + is adopted for the momentum on the K-M line, whereas the negative sign - is chosen for the momentum on the K- Γ line.

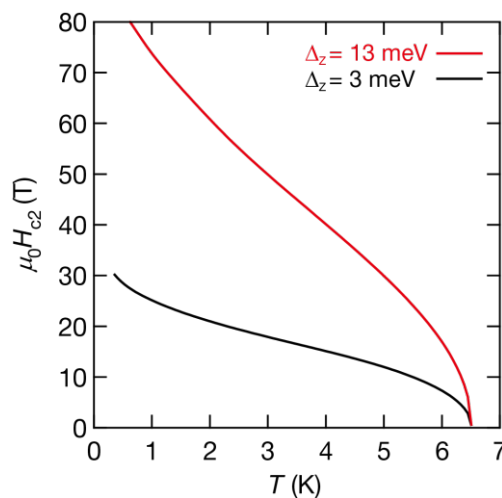
V. Numerical calculation of the Pauli limit

We calculated the Pauli limit, in the present system, based on the BCS model $H = H_0 + H_p + H_l$. Taking into account the Zeeman field by an external magnetic field, $H_p = -\sum_{\mathbf{k}ss'} \mu_B \mathbf{H} \cdot \boldsymbol{\sigma}_{ss'} c_{\mathbf{k}s}^\dagger c_{\mathbf{k}s'}$, and the pairing interaction in the s -wave channel $H_l = V \sum_i n_{i\uparrow} n_{i\downarrow}$, we solved the linearized gap equation $1 - V \chi_{sc}^0(T_c, H_{c2}) = 0$ where V is the pairing interaction and the irreducible superconducting susceptibility as a function of temperature and magnetic field, and determine both T_c and H_{c2} . We focused on the in-plane magnetic field $\mathbf{H} = H \hat{x}$. The irreducible superconducting susceptibility is obtained as

$$\chi_{sc}^0(T, H) = T \sum_{\omega_l} \sum_{\mathbf{k}} \left[G_{\uparrow\uparrow}(\mathbf{k}, i\omega_l) G_{\downarrow\downarrow}(-\mathbf{k}, -i\omega_l) - G_{\downarrow\uparrow}(\mathbf{k}, i\omega_l) G_{\uparrow\downarrow}(-\mathbf{k}, -i\omega_l) \right]$$

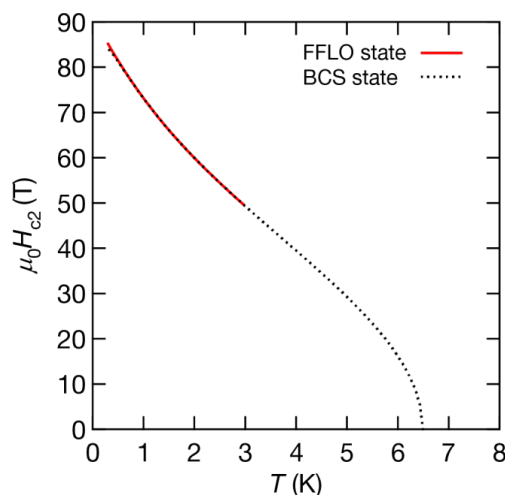
by using the Matsubara Green function, $\hat{G}(k) = (i\omega_l - \hat{H}_0 - \hat{H}_p)^{-1}$. We assumed an attractive interaction $V/t_1 = -2.32$ so that the transition temperature of $T_c = 6.5$ K experimentally observed at zero magnetic field was reproduced.

Supplementary Figure 5 shows the theoretical curves of the Pauli limit in this system. It is shown that the Pauli limit is enhanced by the Zeeman-type SOI to over 70 T at $T = 1$ K. The Zeeman-type spin splitting at the Fermi level of ~ 13 meV plays an essential role in the Pauli limit much higher than the BCS value. Indeed, the smaller Pauli limit than the experimental values is obtained, when we assume a Zeeman-type spin splitting of 3 meV.



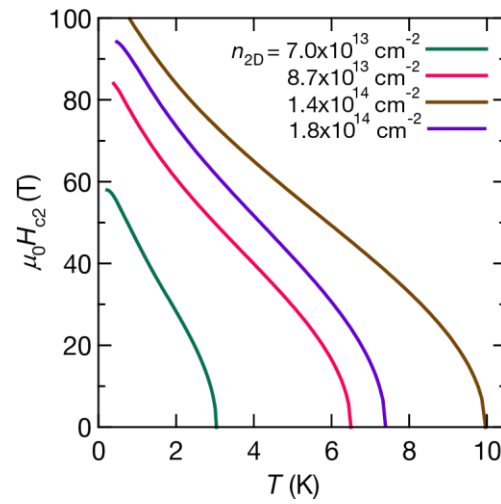
Supplementary Figure 5 | Theoretical curves of the Pauli limit. Red and black curves show the calculated upper critical fields assuming Zeeman-type splittings, Δ_Z , of 13 and 3 meV, respectively.

Our theoretical calculation indeed shows that a FFLO superconducting state (or a helical state) in inter-valley pairing is stabilized in the presence of the Rashba-type SOI. To check the enhancement by the FFLO state, we have performed the numerical calculation of the Pauli limit at both BCS state and FFLO state (Supplementary Fig. 6). Our numerical calculation suggests that the difference between two cases is indeed negligible, and thus the enhancement of the upper critical field due to the FFLO state in our case is negligible by the numerical calculation as shown below, because the Rashba component is extremely small.



Supplementary Figure 6 | Theoretical values of the Pauli limit at the BCS state and a FFLO state.

To discuss the carrier density dependence of H_{c2} in more detail, we show the theoretically calculated value of the Pauli limit as a function of temperature at different carrier densities and T_c as shown in Supplementary Fig. 7. Here, the Rashba component is fixed at 2% of the total spin polarization, as we find no meaningful change in the behaviour of the Pauli limit for Rashba components less than this value. To calculate the Pauli limit, we have also used the same values of the spin splitting which were obtained by our *ab-initio*-based tight-binding supercell calculations and estimated from those values. The spin splitting approximately varies from 9 to 15 eV in the range of the carrier density where superconductivity realizes ($n_{2D} \sim 0.6 - 1.8 \times 10^{14} \text{ cm}^{-2}$), and, in this regime, the K points are much dominantly occupied. As Supplementary Fig. 7 illustrates, the temperature dependence of the Pauli limit at $n_{2D} = 8.7 \times 10^{13} \text{ cm}^{-2}$ is similar to that at $1.8 \times 10^{14} \text{ cm}^{-2}$, although their carrier densities are much different. This similarity is in good agreement with the experimental result (Supplementary Fig. 3, a and b). Combined with experimental data, we concluded that the behaviour of the upper critical field is predominantly controlled by the Zeeman-type SOI and T_c in this range of the carrier density.



Supplementary Figure 7 | Theoretical curves of the Pauli limit at different carrier densities and T_c .

VI. Discrepancy between the theoretical results and experimental results

We here discuss three possible origins for the discrepancy between the theoretical results based on a single-layer tight-binding model and experimental results. One is the weak proximity of carriers to the second MoS₂ layer, in which small amount of carriers is considered to be accumulated. Because the second layer acquires Zeeman-type SOI with an opposite sign to the first layer, the proximity leads to a suppression of SOI and suppresses the enhancement of the Pauli limit. The second possibility is a small misalignment of the pulsed magnetic fields. The pulsed magnetic fields may not be precisely parallel to the surface of the channel, because of an error in the angle or the non-uniformity of pulsed magnetic fields. However, taking the size of device into account, the non-uniformity of pulsed magnetic fields is considered to be less than 0.1 T. The third possibility is impurity scattering effect, which is known to suppress the upper critical field¹⁴. This effect is not included in our calculation for simplicity.

References

1. Yuan, H. T. *et al.* High-density carrier accumulation in ZnO field-effect transistors gated by electric double layers of ionic liquids. *Adv. Funct. Mater.* **19**, 1046–1053 (2009).
2. Yuan, H. T. *et al.* Electrostatic and electrochemical nature of liquid-gated electric-double-layer transistors based on oxide semiconductors. *J. Am. Chem. Soc.* **132**, 18402 (2010).
3. Ye, J. T. *et al.* Superconducting dome in a gate-tuned band insulator. *Science*. **338**, 1193–1196 (2012).
4. Klemm, R. A., Luther, A. & Beasley, M. R. Theory of upper critical-field in layered superconductors. *Physical Review B* **12**, 877–891 (1975).
5. Bauer, E. & Sigrist, M. Non-centrosymmetric superconductors: Introduction and overview. (Springer, Berlin/Heidelberg, 2012).
6. Gor'kov, L. P. & Rashba, E. I. Superconducting 2D system with lifted spin degeneracy: mixed singlet-triplet state. *Phys. Rev. Lett.* **87**, 037004 (2001).
7. Tada, Y., Kawakami, N. & Fujimoto, S. Colossal enhancement of upper critical fields in noncentrosymmetric heavy fermion superconductors near quantum criticality: CeRhSi₃ and CeIrSi₃. *Phys. Rev. Lett.* **101**, 267006 (2008).
8. Tinkham, M. Introduction to Superconductivity, 2nd ed. (Dover, New York, 2004).
9. Zhu, Z. Y., Cheng, Y. C. & Schwingenschlogl, U. Giant spin-orbit-induced spin splitting in two-dimensional transition-metal dichalcogenide semiconductors. *Phys. Rev. B*, **84**, 153402 (2011).
10. Blaha, P., Schwarz, K., Madsen, G., Kvanicka, D. & J. Luitz. WIEN2K program package. Available at <http://www.wien2k.at>.
11. Souza, I. *et al.* Maximally localized Wannier functions for entangled energy bands. *Phys. Rev. B* **65**, 035109 (2001).
12. Mostofi, A. A. *et al.* Wannier90: a tool for obtaining maximally localized Wannier functions. *Comp. Phys. Commun.* **178**, 685–699 (2008).
13. Kunes, J. *et al.* WIEN2WANNIER: from linearized augmented plane waves to maximally localized Wannier functions. *Comp. Phys. Commun.* **181**, 1888–1895 (2010).
14. Bulaevskil, L. N., Guselnov, A. A. & Rusinov, A. I. Superconductivity in crystals without symmetry centers. *Sov. Phys. JETP* **44**, 1243–1251 (1976).